Deformation and Fracture in Micro-stamping Process

Peng Zhang, Michael P. Pereira, Buddhika Abeyrathna, Bernard F. Rolfe, Daniel E.Wilkosz, Peter Hodgson, and Matthias Weiss

Abstract Hydrogen fuel cells could be used to power vehicles with zero emissions. An essential component in the fuel cell is the bipolar plate, which conducts electricity, distributes gas, and removes heat. The metallic bipolar plate that is micro-formed from an ultra-thin stainless-steel sheet is more cost-effective for mass production and more lightweight than the conventional carbon bipolar plates. The scope of this work is to understand the material deformation and ductile fracture behaviour in the micro-stamping process, which is a prototype process that may be used to manufacture bipolar plates. The hardening and fracture models of the ultra-thin stainless-steel sheet were calibrated in the authors' previous work [1] and are implemented in the current process. The accuracy of the FE model is assessed by comparison with experimental trials with regard to material thinning, profile shape, and point of fracture initiation.

Keywords Micro-stamping · Ultra-thin sheet · Bipolar plate · Ductile fracture · FEA

Introduction

The innovation of fuel cells provides a cleaner and more efficient electricity generation technique for future electrification of vehicles. Among all the different types of fuel cells, Proton Exchange Membrane Fuel Cells (PEMFCs) have been successfully commercialised [2] due to their outstanding performance. The Bipolar Plate (BPP) is

---

P. Zhang (✉) · B. Abeyrathna · P. Hodgson · M. Weiss
Institute for Frontier Materials, Deakin University, Waurn Ponds, Pigdons Rd., Geelong, VIC 3216, Australia
e-mail: pen@deakin.edu.au

M. P. Pereira · B. F. Rolfe
School of Engineering, Deakin University, Waurn Ponds, Pigdons Rd., Geelong, VIC 3216, Australia

D. E.Wilkosz
Ford Motor Company, Research and Innovation Center, 2101 Village Rd., Dearborn, MI 48121, USA

K. Inal et al. (eds.), *NUMISHEET 2022*, The Minerals, Metals & Materials Series,
https://doi.org/10.1007/978-3-031-06212-4_6

a key component in a PEMFC. The common shape of the bipolar plate is designed so that it consists of multi-rows of close-spaced micro-channels to maximise the power density of the PEMFC [3]. These micro-channels are necessary to provide reaction sites for the hydrogen and the oxygen. Historically, the material used for the bipolar plate has been graphite [4]. The conventional graphite plate, however, is brittle, expensive, and has high permeability to gas thus requiring additional processing steps; therefore, it is not highly suitable for mass production. The bipolar plate made from stainless steel offers a substitute solution to using its conventional graphite counterpart [4]. Recently, micro-roll forming [3, 5] and micro-stamping [6] have been identified as two potential approaches to produce the bipolar plate using thin stainless steel. The scope of this work is to experimentally and numerically evaluate the material thinning and fracture in micro-stamping conditions that are representative of those used for bipolar plate production.

Material and Methods

Experimental Procedure

The target dimension of one single corrugation of the micro-stamping sample is specified in Fig. 1a and a formed sample is shown in Fig. 1b. This cross-section geometry was chosen based on anticipated forming challenges. The 2D geometry of the experimental tooling used was measured with a non-contact profilometer (Alicona, Austria) for implementation in the FEA in Sect. 2.2.

Industry standard 0.1-mm-thick 316L stainless-steel sheet is stamped between a punch and die to produce seven identical channels that are parallel to each other, as shown in Fig. 1b. The load is applied on the punch using an Instron 500 kN universal tensile machine, the test setup, and schematics of the stamping tools are shown in Fig. 2a. The load frame moves with 5 N/s and is controlled in Bluehill®

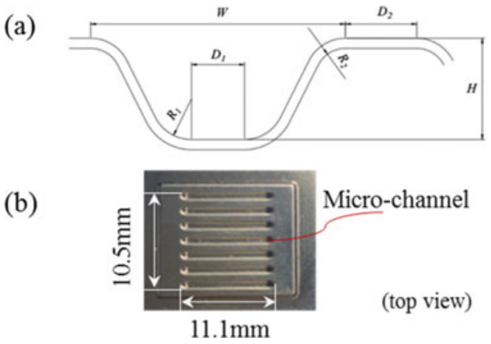

*Symbols in **Fig. 1** (a)*	*Unit: mm*
depth (H)	0.5
span (W)	0.89
punch side radius (R_1)	0.12
die side radius(R_2)	0.12
bottom flat D_1	0.1
top flat D_2	0.8

Fig. 1 **a** Schematic and dimensions of the target corrugation profile **b** a micro-stamped sample

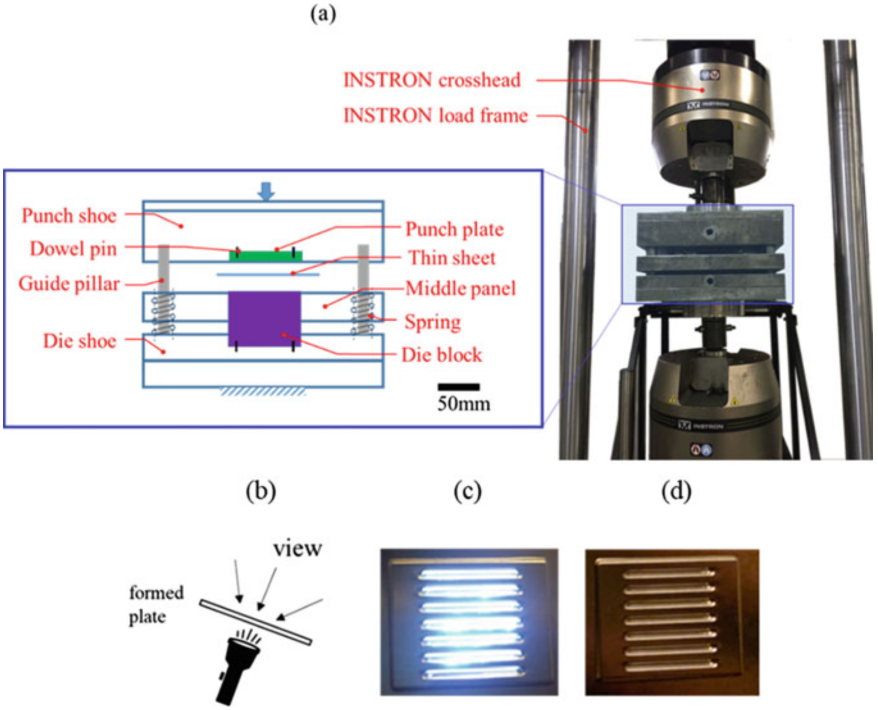

Fig. 2 **a** Stamping tool schematics and the test setup. **b** White light method used to identify cracks and pin holes. Examples of channel patterns formed: **c** failed and **d** successful

(Instron, Ill., USA). After forming, a white light apparatus was used to illuminate the back surface of formed samples, as schematically shown in Fig. 2b. If cracks or pin holes were present the back-side surface light would diffuse through the voids and be visible from the top surface. Examples of a cracked sample and a successfully formed sample are shown in Fig. 2c, d, respectively. The profile shape achievable before fracture initiation is measured with the profilometer on the top surface.

Subsequently, the formed part is cut out from the formed sheet with scissors. The surface of the specimen was cleaned using ethanol, mounted using epoxy resin and cut in sections with an Accutom 50–1 (Struers, Australia). Two section cuts were performed at 1/3 and 2/3 of the corrugation length, as schematically shown in Fig. 3a. The measurement of material thinning is conducted in Image J in the same way as it was previously done for micro-roll formed specimens in [5]. The direction of the microscope observation is schematically shown in Fig. 3b.

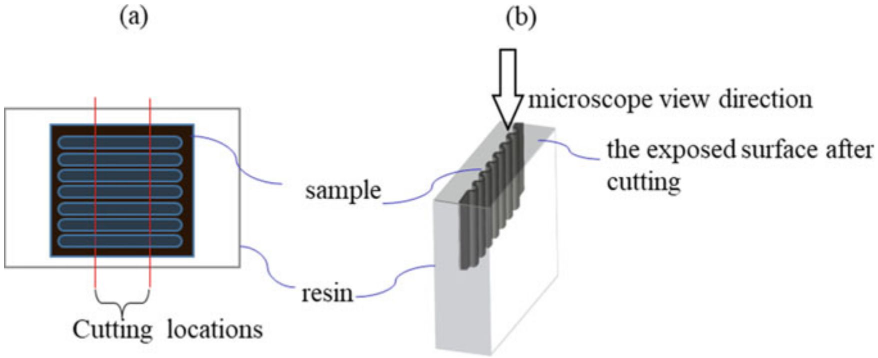

Fig. 3 **a** Schematics of the mounted sample and the cutting locations (in top view) and **b** the exposed surface after the cutting process for microscope examinations

Micro-stamping FEA Model

In all channels, the crack did not initiate from the cavities at two ends (half-spherical shapes), where three-dimensional forming would be presented. In addition, the shape of all corrugations is the same and the major deformation is stretching along the transverse direction. For this reason, the deformation of the sheet metal was simplified as plane strain and the FEA model reduced to a two-dimensional (2D) problem. In lieu of no available CAD information, the 2D geometry of the experimental tool's profile was measured with the profilometer and imported to ABAQUS. For this, a 2D middle cross section on the 3D shape was created to represent the shape of the forming region, as it is shown in Fig. 4. The punch and the die have a periodical geometry, and thus the dimensions of one channel are representable for all seven channels. An approximation of the tool radii was made to build the sketches in ABAQUS so that an analytical rigid model could be used to represent the forming tools. For this, the real geometry was smoothened by a combination of straight lines and regular radii to match the measured tool profile as close as possible. This avoids penetration of the sheet by very small sharp tool features in the FEA.

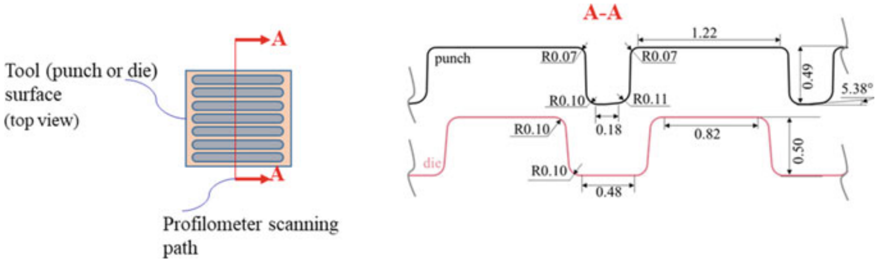

Fig. 4 Schematics of the profilometer scanning path on tools surfaces and the obtained contour of the punch and the die used for simulation

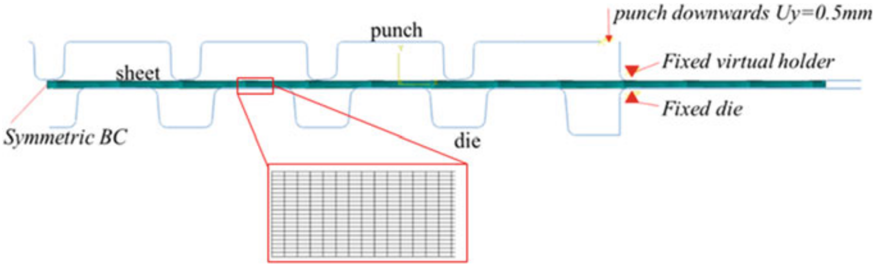

Fig. 5 Model of the micro-stamping process

Due to the symmetry of the load and geometry, half of the pattern was simulated, that is, the punch and die were reduced to 3.5 corrugations. The sheet was meshed with CPE8R elements, which are plane-strain continuum elements with reduced integration, and 20 elements in the thickness direction were used. Previous studies have indicated that in micro-forming, the coefficient of friction (COF) is higher compared to that in conventional forming [7] and a COF = 0.4 was used here. The "surface-to-surface" contact was applied to define the interaction between the sheet and tools. In the forming step, a vertical displacement was applied to the punch while the die and the blank holder remained fixed. The left end of the sheet was constrained by a symmetry boundary condition (BC) while the right end remained free to move, as shown in Fig. 5.

Fracture Model

The plastic hardening behaviour of the sheet material is expressed in Eq. 1, with $\overline{\sigma}$ being the true stress and $\overline{\varepsilon}$ the equivalent plastic strain. The Gurson–Tvergaard–Needleman (GTN) model [8], with its yield function expressed in Eq. 2, is used for the analysis of fracture initiation.

$$\overline{\sigma} = S_0\bar{\varepsilon} + H \tag{1}$$

$$\phi = \left(\frac{\sigma_v}{\tilde{\sigma}}\right)^2 + 2q_1 f \cosh\left(\frac{3}{2}q_2\frac{P}{\tilde{\sigma}}\right) - \left(1 + q_3 f^2\right) = 0 \tag{2}$$

where S_0 and H are the linear hardening parameters; σ_v is von Mises stress; P is the hydrostatic stress; q_1, q_2, q_3 are material parameters; f is the void volume fraction, the rate of which $(\dot{f})$ can be determined with the void growth term $(\dot{f}_{gr})$; and void nucleation term $(\dot{f}_{nucl})$ described in Eq. 3.

$$\dot{f} = \dot{f}_{gr} + \dot{f}_{nucl} \tag{3}$$

Table 1 Parameters used for the simulation

S_N	ε_N	f_N	q_1	q_2	q_3	S_0	H
0.1	0.27	0.05	1.8	1	3.24	2204.2	325.6

The rate of growth based on the law is expressed in Eq. 4, where $\dot{\boldsymbol{\varepsilon}}$ is the plastic strain rate tensor and $\mathbf{I}$ is the identity tensor.

$$\dot{f}_{gr} = (1 - f)\dot{\boldsymbol{\varepsilon}} : \mathbf{I} \tag{4}$$

The nucleation of voids is given by a strain-controlled intensity index A, as expressed in Eq. 5:

$$\dot{f}_{nucl} = A\dot{\bar{\varepsilon}}; \quad A = \frac{f_N}{S_N\sqrt{2\pi}}\exp\left(-\frac{1}{2}\left[\frac{\varepsilon - \varepsilon_N}{S_N}\right]^2\right) \tag{5}$$

where f_N, S_N, and ε_N are the parameters related to void nucleation. The contribution of void volume fraction due to void coalescence is included in the conventional GTN model; however, the coalescence term is neglected here. This is because a sudden load drop (fracture) was found in the thin sheet samples during the calibration test, and thus the gradual degradation of the material's load bearing capacity due to void coalescence can be neglected. The models were calibrated in [1] and the calibrated parameters are listed in Table 1. Fracture is deemed to occur when the void volume fraction f reaches the critical value f_c, which is dependent on the stress triaxiality. The stress triaxiality and the f_c are expressed in Eqs. 6 and 7, respectively.

In general, the stress triaxiality of all the samples varies until fracture occurs. Therefore, the stress triaxiality η was averaged in a range between 0.1 and 0.5 of equivalent plastic strain $\bar{\varepsilon}$. The average triaxiality η_{avg} is calculated with Eq. 6. It is assumed that the computed void volume fraction f (in Eq. 2) of the thin sheet reaches the critical volume fraction f_c when fracture initiates. The relation between f_c and η_{avg} was determined by fitting the various pair data of (η_{avg},f_c) determined by tensile tests with notched thin sheet samples and biaxial stretch forming tests during the calibration process [1].

$$\eta_{avg} = 2.5\int_{0.1}^{0.5} \eta \mathrm{d}\bar{\varepsilon} \tag{6}$$

$$f_c = 4.34{\eta_{avg}}^2 - 3.76 + 0.88 \tag{7}$$

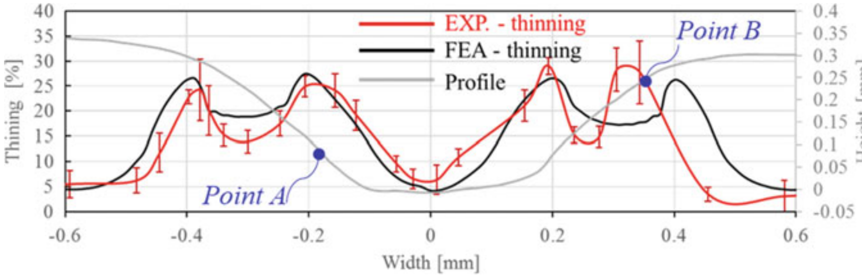

Fig. 6 Thinning prediction for the micro-stamped profile compared to the experimental results (maximum achievable profile)

Results and Discussion

Material Thinning Prediction

The FEA model was used to analyse material thinning at the final punch stroke before fracture. The experimental and the FEA results are illustrated in Fig. 6. The results are overlayed with the maximum achievable profile shape of the top surface before fracture obtained from the experiments (see grey curve in Fig. 6). It is evident that the FEA model captures well the general trends of material thinning, except for some area near the 0.2–0.3 mm region width. The localised thinning observed in this area appears in every row of channels and, therefore, may be due to misalignment between the punch and die which was not captured by the FEA model.

Fracture Model Implementation

The location of the peak equivalent plastic strain changes as the punch moves down, until it begins to stabilise at the left corner of the bottom radius at an equivalent plastic strain of 0.5. When the void volume fraction f at this point reaches the critical constant f_c (Eq. 7) fracture is considered to initiate. This node is located at the left bottom radius in *point A* shown in Figs. 6 and 7. It is noted that this node does not coincide with the fracture initiation *point B* found in the micro-stamping experiments which is located on the right top radius with scattered thinning (*point B* shown in Fig. 6). This may be due to tool misalignment as explained earlier. The average stress triaxiality in *point A* is numerically determined first to enable the use of the parabolic coalescence law (Eq. 5). The stress triaxiality versus the equivalent plastic strain is shown in Fig. 7. Using Eq. 6, the average stress triaxiality is calculated to be $\eta_{\text{avg}} = 0.54$. Implementing $\eta_{\text{avg}} = 0.54$ in the parabolic law of Eq. 7 gives $f_c = 0.12$.

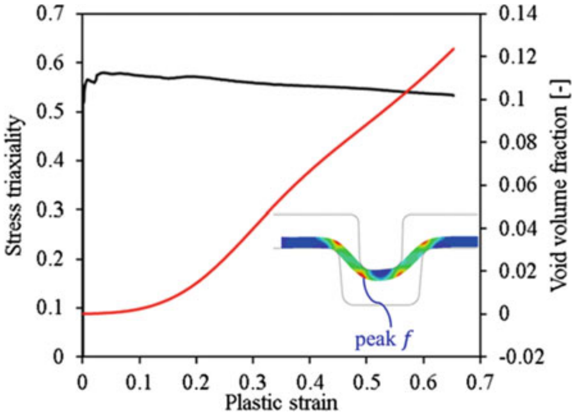

Fig. 7 The stress triaxiality (black line) and the void volume fraction (red) versus the equivalent plastic strain at the critical node (point A)

Using $f_c = 0.12$ in the numerical model of the micro-stamping process suggests safe forming for the full punch stroke of 0.5 mm, as shown in Fig. 8. However, in the experimental trials, fracture initiated at a punch stroke of 0.3 mm (indicated by the blue line in Fig. 8). This discrepancy may be due to a combination of the tool shape inaccuracy, tool misalignment, and the resolution of the model predictions, which need to be further explored. Nevertheless, one attribution is the potential misalignment of the punch and the die in the experimental scenario, which is not included in the numerical model. The experimental thinning results in Fig. 6 suggest that unsymmetrical thinning exists which indicates tool misalignment. However, the FEA model predicts symmetrical thinning because a perfect (i.e. symmetric) alignment of the punch and die is assumed. This represents a less severe forming condition and may explain why fracture is predicted to occur at a lower punch stroke than observed in the experiments.

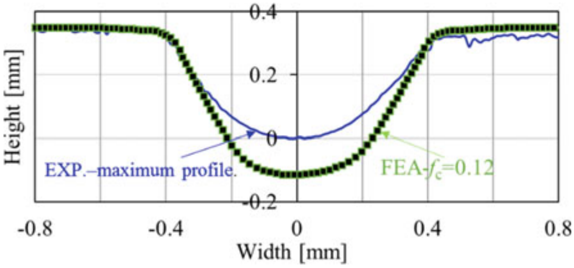

Fig. 8 Comparison of the formed profile at fracture predicted by the FEA and shown by the experimental results (EXP. plot in blue is the profile at fracture initiation). FEA with $f_c = 0.12$ suggests successful forming for the full punch stroke

Conclusion

The micro-stamping process is numerically analysed using a calibrated GTN model. The implementation of a parabolic coalescence model, which estimates the critical volume fraction, f_c, gives a reasonable thinning prediction that correlates well with the experiments. The FEA fracture initiation is defined to initiate on a critical node that shows a critical void volume fraction. However, it was found that the critical node predicted by the model does not correlate with the fracture initiation location found in the experiments. This discrepancy may be due to a combination of tool shape inaccuracy and tool misalignment that was not captured in the FEA model. In addition, the maximum depth of the channel that can be safely formed is overestimated. Future study will investigate the effect of the tool radius and alignment on the thinning and the level of void volume fraction in the micro-stamping process, to further improve the fracture model.

References

1. Zhang P, Pereira M, Rolfe B, Wilkosz D, Abeyrathna B, Hodgson P, Weiss M (2020) Plastic instability and fracture of ultra-thin stainless-steel sheet. Int J Solids Struct 202:699–716
2. Gerbec M, Jovan V, Petrovčič J (2008) Operational and safety analyses of a commercial PEMFC system. Int J Hydrogen Energy 33:4147–4160. https://doi.org/10.1016/j.ijhydene.2008.04.063
3. Zhang P, Pereira M, Rolfe B, Daniel W, Weiss M (2017) Deformation in Micro Roll Forming of Bipolar Plate. J Phys Conf Ser 896:012115. https://doi.org/10.1088/1742-6596/896/1/012115
4. Hermann A, Chaudhuri T, Spagnol P (2005) Bipolar plates for PEM fuel cells: a review. Int J Hydrogen Energy 30:1297–1302. https://doi.org/10.1016/J.IJHYDENE.2005.04.016
5. Abeyrathna B, Zhang P, Pereira MP, Wilkosz D, Weiss M (2019) Micro-roll forming of stainless steel bipolar plates for fuel cells. Int J Hydrogen Energy 44:3861–3875. https://doi.org/10.1016/J.IJHYDENE.2018.12.013
6. Leng Y, Ming P, Yang D, Zhang C (2020) Stainless steel bipolar plates for proton exchange membrane fuel cells: materials, flow channel design and forming processes. J Power Sour 451:227783. https://doi.org/10.1016/j.jpowsour.2020.227783
7. Geiger M, Kleiner M, Eckstein R, Tiesler N, Engel U (2001) Microforming. CIRP Ann Manuf Technol 50:445–462. https://doi.org/10.1016/S0007-8506(07)62991-6
8. Dassault Systèmes (2014) Porous metal plasticity. In: Abaqus 6.14-Abaqus theory guid. Dassault Systèmes Simulia Corp., Providence, RI